Space Charge Accumulation and Its Impact on High-Voltage Power Module Partial Discharge under DC and PWM Waves: Testing and Modeling

Yalin Wang, Member, IEEE, Yi Ding, Zhao Yuan, Hongwu Peng, Jiandong Wu, Member, IEEE, Yi Yin, Member, IEEE, Tao Han, Member, IEEE, and Fang Luo, Senior Member, IEEE

***Abstract*—Emerging applications of compact high-voltage SiC modules pose strong challenges in the module package insulation design. Such SiC module insulations are subjected to both high voltage DC and PWM excitations between different terminals during different switching intervals. High d*V*/d*t* strongly interferes with partial discharge (PD) testing as it is hard to distinguish PD pulses and PWM excitation induced interferences. This paper covers both the testing and modeling of PD phenomena in high-voltage power modules. A high d*V*/d*t* PD testing platform is proposed, which involves a Super-High-Frequency (SHF, >3GHz) down-mixing PD detection receiver and a high-voltage scalable square wave generator. The proposed method captures SHF PD signatures and determines PDIV for packaging insulation. Using this platform, this paper provides a group of PDIV comparisons of packaging insulation under DC and PWM waveforms and discloses discrepancies in these PDIV results with respect to their excitations. Based on these PD testing results, the paper further provides a model using space charge accumulation to explain the PD difference under DC and PWM waveforms. Both simulation and sample testing results are included in this paper to support this hypothesis. With this new model, the paper includes an updated insulation design procedure for high-voltage power modules.**

***Index terms*—Power module, space charge, partial discharge, packaging, encapsulation, insulation.**

I. Introduction

HIGH voltage power modules, especially SiC power modules, are required to have high power density that leads to a smaller package and higher operating voltage, which brings severe challenges to packaging insulation [1]. Partial discharge (PD) is regarded as an indicator of premature insulation failure, and the detection of PD plays a significant role in the condition monitoring of high-voltage power modules.

However, three main gaps between the academic PD research and industrial application should be urgently bridged for high-voltage power modules. First, the current PD testing standards such as IEC 61287 for power modules (mostly for Si modules) are based on the PD test under power frequency sinusoidal voltage, which does not agree with the actual applied electric stress to the power module packaging insulation. Take the widespread commercial half-bridge high-voltage module as an example. A half-bridge power module usually contains two sets of MOSFET or IGBT chips in series and three power terminals as T_1, T_2, and T_3, which connect to the positive terminal of a DC source, output load, and negative terminal of the DC source, respectively. These three terminals are connected to metal pads on the substrate, and the metal pads are isolated with insulating materials to avoid failure. The voltage across T_1 and T_3 is DC, whereas the voltage across T_1- T_2 and T_2-T_3 is PWM waves. The form of electric stress affects the local electric field distribution in the packaging insulation, thereby results in different PD characteristics [2]. Therefore, the PD characteristics of power module insulation under DC and PWM excitation cannot be obtained from the power frequency PD test defined by existing standards, and they should be thoroughly investigated to update these standards.

Second, PD detection for high-voltage power module packaging insulation under PWM waves is challenging. Since the SiC/GaN semiconductor can switch with very short transient time, the PWM waves (square pulses) with ultra-high d*V*/d*t* will cause non-negligible electromagnetic interference and high displacement current that flows through the packaging insulation due to its capacitive nature, which largely influences the widely used electrical signal based PD detection methods, such as high-frequency current transformer (HFCT). Especially, the PDs often initially occur at the rising and falling edges, the electromagnetic interference and displacement current just occur at this time region and will interfere and cause errors for PD detection. To avoid this interference, researchers proposed non-electrical PD detection methods such as acoustic-based and optical-based methods [3-5]. However, these methods either have inherent flaws or not suitable for practical PD monitoring of high-voltage power modules, which will be discussed later.

Yalin Wang is with Department of Electrical Engineering, University of Arkansas, AR, Fayetteville, USA, the Department of Electrical Engineering, School of Electronic Information and Electrical Engineering, Shanghai Jiao Tong University, Shanghai, China (e-mail: wangyalin2014@sjtu.edu.cn).
Yi Ding, Jiandong Wu, and Yi Yin are with the Department of Electrical Engineering, School of Electronic Information and Electrical Engineering, Shanghai Jiao Tong University, Shanghai, China, Key Laboratory of Control of Power Transmission and Conversion (SJTU), Ministry of Education, Shanghai, China (e-mail: 2018-ee-dingyi@sjtu.edu.cn, jdwu@sjtu.edu.cn, yiny@sjtu.edu.cn).
Zhao Yuan and Hongwu Peng are with the Department of Electrical Engineering, University of Arkansas, AR, Fayetteville, USA (e-mail: zhaoyuan@uark.edu, hp013@uark.edu).
Tao Han is with the Department of Instrument Science and Engineering, School of Electronic Information and Electrical Engineering, Shanghai Jiao Tong University, Shanghai, China (e-mail: than@sjtu.edu.cn).
Fang Luo is with the Department of Electrical and Computer Engineering, Stony Brook University (SUNY at Stony Brook), Stony Brook, NY, USA (e-mail: fang.luo@stonybrook.edu).
(Corresponding author: Fang Luo.)

Third, the PD mechanism for solid insulation in power modules has not been fully explored. Voids or air bubbles in solid insulation are the most investigated situations, but the state of art manufacturing technique can limit the voids to a quite low level, hence, the solid insulation PD is more prominent. The failure of packaging insulation is related to many factors, such as the type of electric stress, electrical properties of the insulating material, structure of the packaging, *et al* [6]. The high-voltage power module packaging insulation commonly uses polymeric encapsulation materials and ceramic substrates. However, polymeric materials are vulnerable to space charge accumulation especially under DC situations due to the local states in the forbidden bands (shallow and deep traps) [7]. Space charge accumulation causes electric field distortion, accelerates insulation degradation, and leads to PD then completely breakdown [8, 9]. Due to the irregular insulation structure of the power module package, the triple-point among encapsulant, metal pads, and ceramic substrate is where the highest local electric field appears [10, 11]. Charges can be injected from the triple-point at metal pads of the substrate and then accumulated in the insulation around metal edges. The accumulated charges distort the local electric field, which in turn affects PD characteristics. The space charge issue is widely acknowledged in HVDC equipment such as HVDC cables, but it has not aroused much attention and is not considered in high-voltage power module packaging design.

The contributions of this paper are as follows:

(1). This study proposes a high dV/dt PD testing platform that involves a Super-High-Frequency (SHF)-down-mixing PD detection system and a high-voltage scalable square wave generator. The PD detection method has the advantage of both anti-interference characteristics and convenient implementation.

(2). A space charge accumulation model is introduced to explain the partial discharge inception voltage (PDIV) difference under DC and PWM excitation. With this new model, an improved insulation design procedure combining experimental and simulation results is proposed for high-voltage power modules.

The rest of this paper is organized as follows: Section II introduces a PD testing platform containing a high-voltage square pulse generator based on a supercascode structure and an SHF-down-mixing PD detecting system. Section III presents PD experiment results of power module packaging insulation under DC and square pulse conditions. Section IV describes the space charge measurement and modeling of power module packaging insulation, and a tentative high-voltage power module packaging insulation design procedure is proposed. Section V concludes this paper.

II. Partial Discharge Testing Platform for Power Module Packaging Insulation

The most widely used commercial power module structure is the half-bridge module, whose structure is shown in Fig. 1. A PD testing platform, including a high-voltage (10 kV) square pulse generator using supercascode structure with off-shelf SiC devices, and a contactless PD monitor using SHF signatures

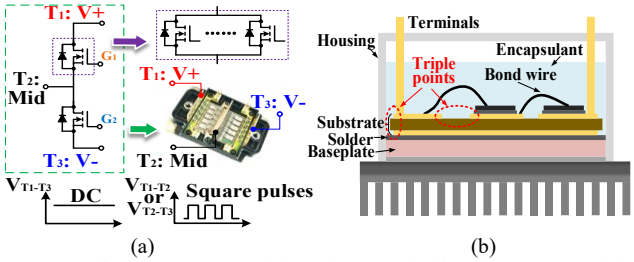

Fig. 1. Half-bridge power module package. (a) *half-bridge power module and electric stress between power terminals* (b) *schematic of the cross-section of a power module*

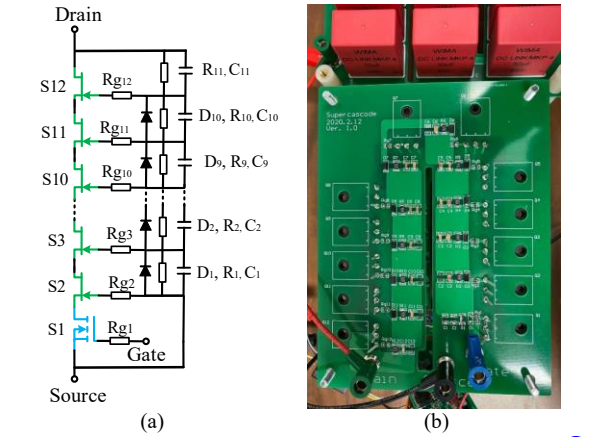

Fig. 2. Supercascode cell. (a) schematic (b) photograph (c)high voltage square pulse output

from the PD event, is built to detect PDs in high-voltage power module insulation under DC and PWM excitations.

A. High-Voltage Square Pulse Generator Based on Supercascode Structure

A modified supercascode structure, as shown in Fig. 2, is adopted to realize this high-voltage square pulse generator. Each high voltage generator contains two sets of supercascode high-voltage switches. Each supercascode high-voltage switch consists of eleven series-connected 1.2 kV SiC JFETs and a SiC MOSFET as the gate, and a paralleled *RC* voltage-balancing network to achieve a high-voltage switching up to 10 kV [12-14]. The SiC JFETs are normally on, while the switching duty cycle is controlled by the SiC MOSFET. To avoid over-voltage on the gate of the bottom JFET, the gate of S2 is connected to the source terminal of S1. This high-voltage generator provides 7.5 kV square pulses with 50 kV/μs dV/dt , as shown in Fig. 2(c). Fig. 2(c) also illustrates the displacement current and

electromagnetic interference collected by high-frequency current probe (Pearson electronics, Model 4100) and wideband antenna (Kelianda Tech, Model CF-0118B), when applying this 7.5 kV square pulse on to the DBC DUT with several pF equivalent capacitance. The supercascode cells are immersed in dielectric oil to prevent any PD event from the pulse generator itself.

B. Partial Discharge Detection Based on SHF and Down-Mixing Principle under Square Pulse with High dV/dt

(1). Detection Mechanism

PD detection for high-voltage power module packaging insulation under square pulse with a high d*V*/d*t* becomes challenging (interference at the pulse edges are shown in Fig. 2). Non-electrical PD detection methods such as acoustic-based and optical-based methods [4-6] can limit interference caused by the short transient time of high-voltage square pulses, but they also have inherent flaws that prevent their widespread practical online use for power modules, as summarized in Table I. The SHF method presented in this paper belongs to the electromagnetic method. To characterize the interference signal, a wideband horn antenna with a bandwidth from 100 MHz to 10 GHz is used and the measured interference (without amplification) caused by high-voltage square pulses are shown in Fig. 3. The spectrum of the interference caused by square pulses is mainly distributed below 3 GHz, which will interfere with the electrical detection method such as pulsed current method and ultra-high frequency (UHF) method. According to IEC 61934 standard, it is recommended to increase detecting frequency and use a high-pass filter to eliminate the overlapping spectrum between the interference and PD signal. However, increasing the detecting frequency results in a higher requirement for signal sampling and processing speed. To solve this problem properly, an SHF-down-mixing PD detection method is proposed. It should be noted that the down-mixing principle has been vastly used in signal processing research such as analog videotape recording [15] and optical heterodyning [16], but the combination of SHF detection and down-mixing to achieve PD detection under square waves has not been reported.

The spectrum of the PD signals above 3 GHz is less interfered and they can be detected by an SHF (> 3 GHz) antenna and high-pass filter. In this frequency band, the electromagnetic interference caused by the power module turning on and off (rising and falling edge of the square wave) will not occur, and the interference caused by communication signals such as mobile phone signals will be greatly reduced, thereby improving the reliability of the measurement results. Moreover, the down-mixing principle is adopted to shift the spectrum of SHF PD signal (> 3 GHz) to a lower frequency band (<1 GHz in this study) for the convenience of signal acquisition.

The essence of down-mixing is to multiply two signals with different frequencies. Assuming that two signals with frequencies f_1 and f_2 are mixed. After mixing, two signals with the difference-frequency and the sum-frequency of the input signal will appear, as shown in Fig. 4.

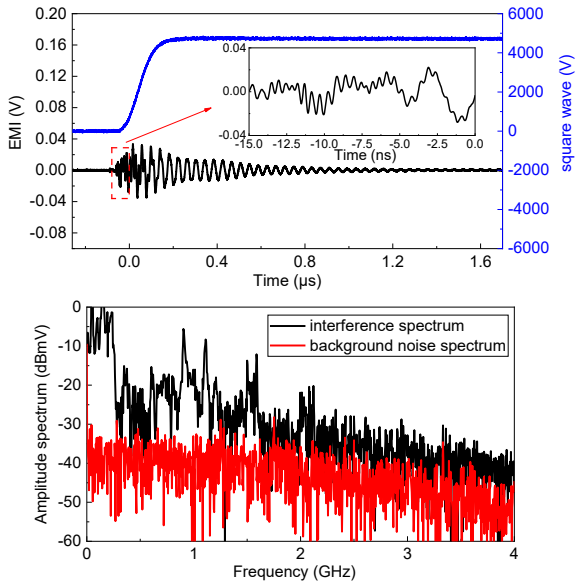

Fig. 3. Interference measured by wideband horn antenna and its spectrum from FFT (from a RF shielded room)

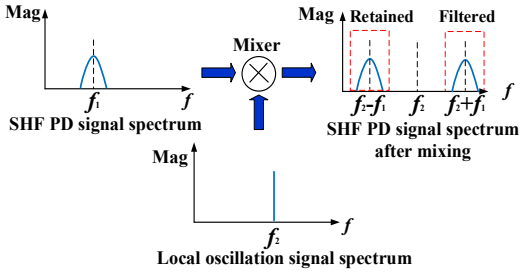

Fig. 4. Principle of the down- mixing technique.

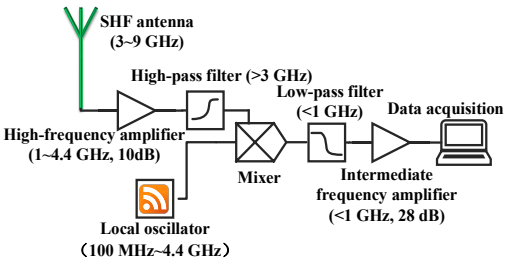

Fig. 5. Schematic of the SHF PD detection system.

$$\cos(2\pi f_1 t)\cos(2\pi f_2 t) = 1/2\{\cos[2\pi(f_1+f_2)t]+\cos[2\pi(f_1-f_2)t]\} \quad (1)$$

Then, a low-pass filter is used to eliminate the sum-frequency (f_1+f_2) signal and keep the difference-frequency (f_1-f_2) signal. The SHF PD signal and a sinusoidal local SHF oscillation signal are input to the mixer, the difference-frequency signal can be obtained and the spectrum of the SHF signal is moved to the lower frequency band. This method not only takes advantage of the anti-electromagnetic interference characteristic in the SHF band but also reduces the difficulty of signal acquisition. In this study, the PD signal received by the SHF antenna is filtered by a high-pass filter and mixed with the local oscillation signal with ~3 GHz. The down-mixed signal is then retained by a low-pass filter to characterize the PD.

TABLE I
PROS AND CONS OF VARIOUS PD DETECTION METHODS UNDER SQUARE WAVES [3-5]

PD detection methods		Frequency band	Pros	Cons
Non-electrical method	Acoustic method	20 kHz-2 MHz	1. Electrical interference immunity 2. Possible for PD location	1. Not quantitative 2. Slow response 3. Reflection-caused error
	Optical method	3×10^{14} Hz-2×10^{15} Hz	Highly electrical interference immunity	1. Must in dark environment 2. Point to tested sample without barrier
	Chemical method	Not applicable	Highly electrical interference immunity	1. Too slow response 2. Need enough PD-induced byproduct
Electrical method	Pulsed current method/ HFCT	3 MHz-30 MHz	1. Quantitative 2. Well-defined in standards	1. Susceptible to displacement current 2. Slow response
	Electromagnetic method/ UHF	300 MHz-3 GHz	1. Relative anti-interference 2. Contactless	1. Not quantitative 2. Need fast data acquisition

The frequency of local oscillation signal f_2 should be higher than the highest frequency of the interference signal to make sure the interference would not be incorporated in the mixed signal. f_2 should also be chosen close to the energy-concentrated frequency component of the partial discharge signal in the SHF band to have a high signal-to-noise ratio.

(2). Detection System

The PD detection system is composed of an SHF sensor (omnidirectional antenna with bandwidth from 3 to 9GHz designed by authors), a high-frequency amplifier (1 to 4.4 GHz, 10dB), a high-pass filter (LTCC structure, >3 GHz, VSWR 20:1 at stopband), a mixer (double-balanced, 10 MHz to 4.4 GHz), an intermediate frequency amplifier (0.5 to 2.5 GHz, low noise, 28dB), and a low-pass filter (LTCC structure, DC to 1 GHz, VSWR 20:1 at stopband), as shown in Fig. 5. PD signals are picked up by the antenna (10 cm away from the tested sample), and the signal is amplified and filtered to eliminate interference. The cut-off frequency of the high-pass filter should be higher than 3 GHz, the stop-band should contain the most frequency components of the interference signal. The filtered SHF signal is input to the mixer, and the local oscillator generates a sinusoidal signal with a frequency around 3 GHz (the frequency can be properly tuned based on the quality of the final output PD signal). Through the low-pass filter and the intermediate frequency amplifier, the difference-frequency signal whose frequency is much lower than 3 GHz is output to an oscilloscope. For the low-pass filter, the cut-off frequency depends on the frequency component of the partial discharge signal in SHF band. It is usually a little higher than the frequency difference between f_2 and the energy−concentrated frequency component of the partial discharge signal in SHF band. To avoid EMI from other sources and the environment, an AC line filter is used to filter the common mode and differential mode noise from the power supply. Moreover, the signal processing circuit and controlling circuit are shielded by a metal case to avoid environmental interference.

(3). Applicability of the SHF-Down-Mixing Method

The main reason for proposing the SHF-down-mixing method is to solve the PD detection under fast square waves which is the case of wide bandgap high-voltage power modules. The initial PD usually occurs at or near the rising/falling edge of the square wave when evaluating PDIV. The interference signal caused by square wave also occurs at this time, which is the most obstacle interfering with the commonly used PD detection methods. It should be pointed out that PD detection is related to many aspects such as the characteristics of noise and PD signal. In this paper, the DBC substrate with silicone encapsulation is tested. The equivalent capacitance of the tested DBC is around several pF and PDs occur at the "triple-point" among DBC copper corner, ceramic layer, and encapsulant. The PD magnitudes of these tested samples are from tens pC to several nC according to the preliminary experiment. It is noted that the PD in solid insulation may tend to have more high-frequency components compared with that in air, which makes it suitable to use the SHF-down-mixing method for power module packaging insulation. Another key factor that influences the applicability of the SHF-down-mixing method is the noise characteristics. In this paper, the supercascode square wave generator with ~50 kV/μs dV/dt is used to apply PWM excitation. It should be pointed out that the change rate of the PWM excitation, equivalent capacitance of the tested sample, and the structure and parasitic parameters of the setup all affect the level of electromagnetic interference and displacement current. The higher the dV/dt and equivalent capacitance of the tested sample, the larger the displacement current. The higher the dV/dt, the more high-frequency component the electromagnetic interference. In summary, the SHF-down-mixing method is appropriate to detect PD that has SHF components and the interference mainly resides under 3 GHz.

III. PARTIAL DISCHARGE DETECTION OF POWER MODULE PACKAGING INSULATION UNDER DC AND SQUARE PULSES

DBC substrates with silicone encapsulants are fabricated as the tested samples as shown in Fig. 6. The encapsulant is cured in a vacuum chamber for 1 hour to eliminate air bubbles [17]. The high-voltage DC and square pulses (10 kHz with 200 ns transition time and 10% duty cycle) are applied to two neighboring copper traces on the tested substrate samples, and the PDIV is recorded 10 times on each condition to obtain a statistical distribution. The PD detection system is verified to be PD-free without connecting tested samples at the full range output voltage. Besides, the system is tested to have at least 20 pC sensitivity for the setup in this study. As known to all, the pulsed current signal has a direct relation with discharge quantity. However, for the electromagnetic method, the magnitude of the PD signal is related to many factors such as discharge current, antenna properties, and position of the antenna. It should be noted that although the magnitude of the

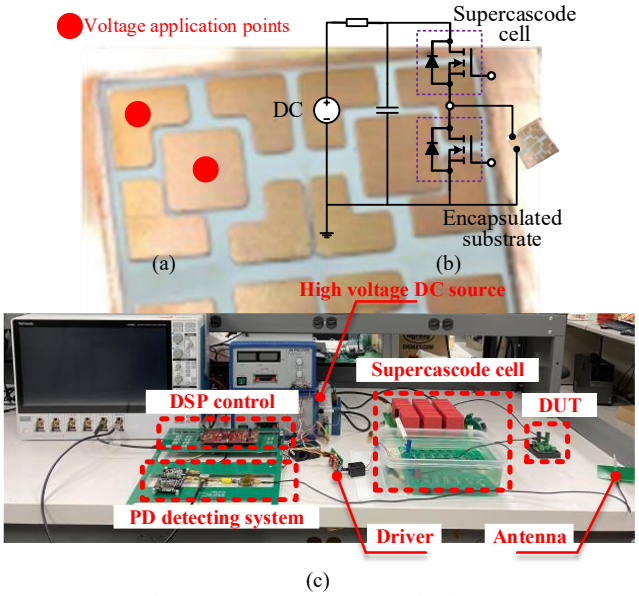

Fig. 6. Partial discharge experiment. (a) tested substrate (b) schematic of experimental setup (C) photograph of experimental setup

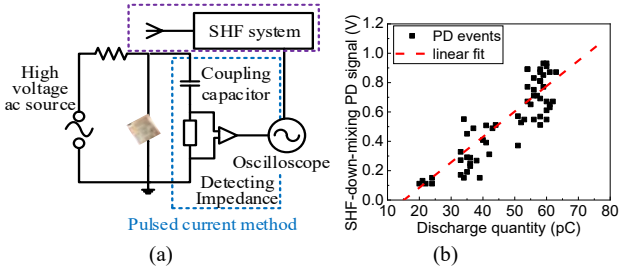

Fig. 7 Sensitivity experiment. (a) Schematic of experiment setup (b) sensitivity of SHF-down-mixing PD signal

SHF-down-mixing PD signal has no direct relation with discharge quantity, it is possible to correlate these two for a certain experiment setup to show a general trend [18]. Since the pulsed current method or HFCT is not suitable to detect PD under square waves, the comparison between the proposed SHF method and pulsed current method is performed under ac voltage just to verify the sensitivity. As shown in Fig. 7, the magnitude of the pulsed current PD signal and that of the SHF-down-mixing signal are highly correlated. The SHF-down-mixing output has a linear relationship with the discharge quantity. It is also noted that the minimum discharge quantity for the tested sample is ~20 pC, which means the SHF-down-mixing method at least has ~20 pC sensitivity for the tested packaging insulation in the setup of this study.

The typical detected signal is shown in Fig. 8(a). The SHF PD signal is quite clean and it just appears at the end of the rising edge of the square pulse where the initial PD always occurs. To verify the down-mixing effect, the spectrum of the SHF PD signal before and after down-mixing is compared, as shown in Fig. 8(b). The spectrum over 3 GHz of the SHF signal is successfully transferred to the frequency below 1 GHz, and the PD signal after down-mixing has a higher signal-to-noise ratio.

The PDIV results are shown in Fig. 9 and analyzed by the two-parameter Weibull distribution [19]:

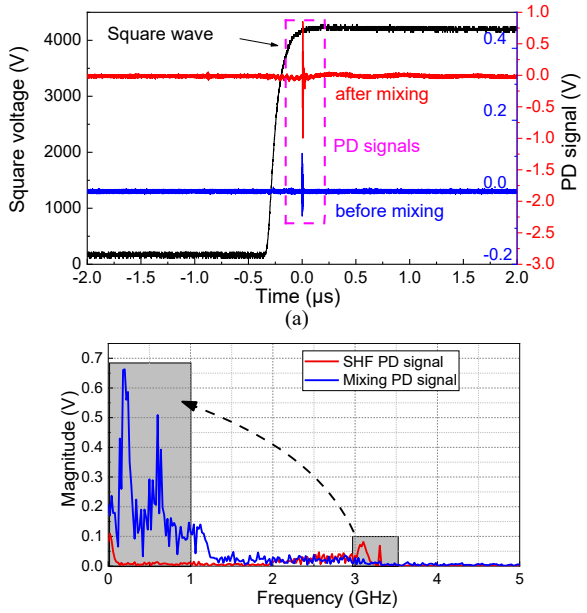

Fig. 8 Typical measured SHF PD signals. (a) SHF PD signals of the tested sample before and after down-mixing (b) spectrum of SHF PD signal before and after down-mixing from FFT

$$P(U_i) = 1 - \exp[-(\frac{U_i}{\alpha})^{\beta}] \qquad (2)$$

where P is a cumulative failure probability, U_i is the measured PDIV under high-voltage DC or square pulse, α is the scale parameter (voltage corresponding to a 63.2% cumulative probability), and β is the shape parameter indicating the distribution width (the smaller the value of β the greater the data scattering). After transformation, equation (2) can be expressed:

$$\lg\{-\ln[1-P(U_i)]\} = \beta \lg U_i - \beta \lg \alpha \qquad (3)$$

Therefore, a linear fit of $\lg\{-\ln[1-P(U_i)]\}$ with respect to $\lg U_i$ gives the scale parameter α and shape parameter β. The PDIV of the tested samples can be estimated by the scale parameter. It is found that the PDIV under square pulse is lower than that under DC stress (~90%) for both 0.35 and 0.5 gap distance, as shown in Table II. This may be related to the space charge accumulation. It can be inferred that during HVDC application, space charges are constantly injected and trapped in the vicinity of triple-point. The charges decrease the electric field in this area, thereby increasing the PDIV compared to that under square pulse since the charges are shortly injected and extracted or decayed during the voltage-off state.

To explain it, space charge experiments are performed on encapsulant material and space charge simulation for the power module packaging structure is investigated in section IV.

IV. Measurement and Modeling of Space Charge in Power Module Packaging Insulation

A. Space Charge Measurement

The pulsed electro-acoustic (PEA) method is used to measure space charge, as shown in Fig. 10. The tested flat sample is

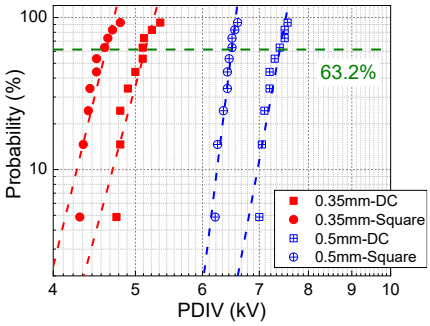

Fig. 9 Weibull distribution of the PDIV of the tested sample with different trace distances

TABLE II
WEIBULL PARAMETERS OF THE TESTED SAMPLES

Metric	DC		Square pulse	
	0.35 mm	0.5 mm	0.35 mm	0.5 mm
scale parameter α (kV)	5.11	7.38	4.60	6.48
shape parameter β	28.38	41.06	31.70	60.20

applied high voltages to accumulate space charge and a nanosecond pulse is also applied to stimulate the vibration of space charge. Then the stimulated mechanical wave travels to the cathode and induces electrical signals by a piezo transducer made of PVDF. The electrical signal then is amplified and recorded by an oscilloscope. In this way, the spatially distributed space charge is transferred to the temporal electrical signal. Details about the PEA method and equipment can be referred to [20]. The same silicone encapsulant used in the PD experiment is fabricated as a flat film with ~300 μm thickness for space charge measurement, as shown in Fig. 11. A step-up voltage from 3 to 15 kV/mm is applied to the sample for every 1800 s and then short-circuited for 3600 s.

The spatial and temporal distributions of space charges in silicone samples are shown in the color-coded form in Fig. 12(a). Homocharges appear in the vicinity of the cathode and anode. The injection depth of space charge increases and more charges are accumulated with the increase in the applied electric field. It is worth noting that there are still quite amount of charges left even after 3600 s short-circuit, showing the space charge is hard to escape from traps even after a long time. According to Poisson's equation, the electric field distribution inside the sample can be recovered from the measured space charge:

$$E(x,t)=\frac{1}{\varepsilon}\int_0^x \rho(x',t)\mathrm{d}x' \qquad (4)$$

where E is the electric field strength, ε is the permittivity of the material, x is the distance to the electrode (cathode), ρ is charge density measured in the sample. The calculated electric field distribution is shown in Fig. 12(b). It can be observed that the electric field around the electrode is decreased but the field between the accumulated positive and negative charges is increased (even higher than the applied electric field). As the applied voltage increases and the charge injection intensifies, the electric field distortion is getting worse. This is because the injected charges serve as sources and affect the local electric field strength around them. Therefore, space charge accumulation has an important effect on the electric field

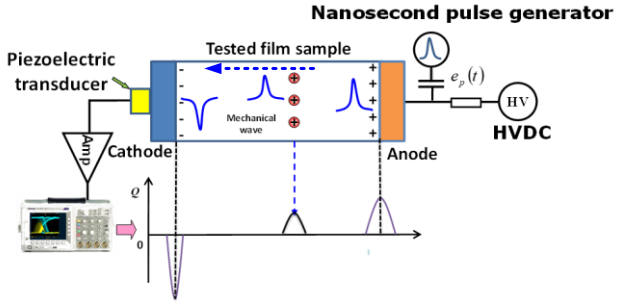

Fig. 10. Schematic of PEA space charge measurement

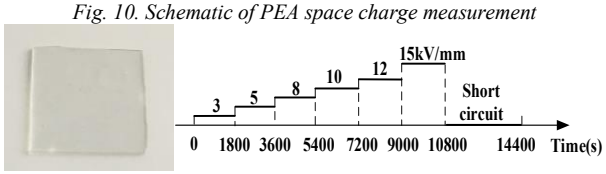

Fig. 11. Space charge measurement setup. (a) photograph of the silicone encapsulant sample (b) voltage application procedure

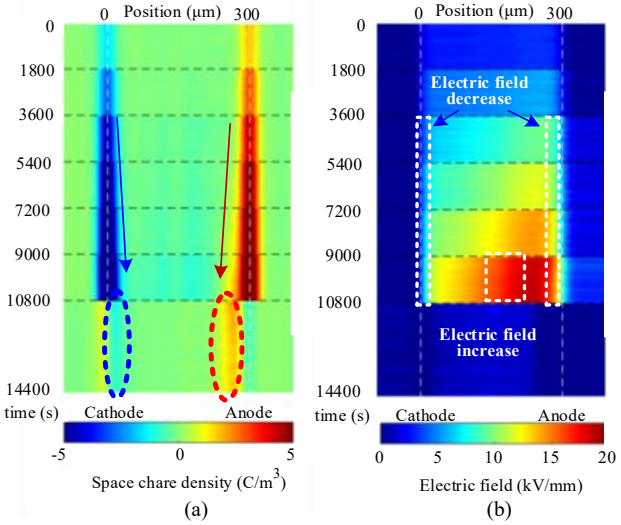

Fig. 12. Space charge measurement results. (a) space charge distribution (b) electric field distribution

distribution inside the sample. Space charge is the main reason for the distortion of the internal electric field of the material under DC high voltage.

The current space charge measurement technique cannot be applied to complicated insulation structures such as power module packaging insulation. The bipolar charge transport model, which considers the physical process of charge injection, extraction, trapping, detrapping, and recombination has been proposed to simulate space charge behavior [21]. In this paper, the model is extended to two-dimensional situations and is combined with the finite element method (FEM) to simulate the space charge dynamics in power module packaging insulation.

B. Space Charge and Electric Field Simulation Based on Bipolar Charge Transport Model

(1). Bipolar charge transport model

Space charges are essentially electrons or holes captured by traps in insulation. Electrons and holes that are either trapped or

mobile are the investigated variables in the model. The electrons and holes can be injected from electrodes and then continuously get trapped, detrapped, and gradually transport into the bulk of the insulation. The focus of the model is to numerically solve partial differential equations (position and time variables are coupled: x, y, and t) that describe the behavior of electrons and holes. The equations contain the transport equation, Poisson's equation, and the continuity equation [21]:

$$\begin{cases} j_a(x,y,t) = \mu_a n_a(x,y,t)E(x,y,t) - D_{fa}\nabla n_a(x,y,t) \\ \nabla E(x,y,t) = \dfrac{\rho(x,y,t)}{\varepsilon} \\ \dfrac{\partial n_a(x,y,t)}{\partial t} + \nabla j_a(x,y,t) = s_a(x,y,t) \end{cases} \tag{5}$$

where the subscript a can be any charge type ($e\mu$ for mobile electrons, et for trapped electrons, $h\mu$ for mobile holes, and ht for trapped holes). μ_a is the charge mobility, n_a is the charge density of any type, j_a is the current density, ρ is the net charge density at any position and time, s_a is the source term, representing the charge density variation due to trapping, detrapping, and recombination. The source terms for trapped and mobile electrons and holes can be expressed as [21]:

$$\begin{cases} s_{ht} = -S_1 \cdot n_{ht} n_{e\mu} - S_0 \cdot n_{ht} n_{et} + B_h \cdot n_{h\mu}\left(1 - n_{ht}/n_{oht}\right) - D_h \cdot n_{ht} \\ s_{h\mu} = -S_2 \cdot n_{h\mu} n_{et} - S_3 \cdot n_{h\mu} n_{e\mu} - B_h \cdot n_{h\mu}\left(1 - n_{ht}/n_{oht}\right) + D_h \cdot n_{ht} \\ s_{et} = -S_2 \cdot n_{h\mu} n_{et} - S_0 \cdot n_{ht} n_{et} + B_e \cdot n_{e\mu}\left(1 - n_{et}/n_{oet}\right) - D_e \cdot n_{et} \\ s_{e\mu} = -S_1 \cdot n_{ht} \cdot n_{e\mu} - S_3 \cdot n_{h\mu} n_{e\mu} - B_e \cdot n_{e\mu}\left(1 - n_{et}/n_{oet}\right) + D_e \cdot n_{et} \end{cases} \tag{6}$$

where S_i is the recombination coefficient, B_e and B_h are the trapping coefficients, D_e and D_h are the detrapping coefficients, n_{oet} and n_{oht} are the density of the trap. The schematic of trapping, detrapping, and recombination in the energy band is shown in Fig. 13. The charge injection can be described as:

$$\begin{cases} j_h(x_0,y_0,t) = AT(x_0,y_0,t)^2 \exp\left[\dfrac{-ew_{hi}}{kT(x_0,y_0,t)}\right]\exp\left[\dfrac{e\sqrt{\dfrac{eE(x_0,y_0,t)}{4\pi\varepsilon}}}{kT(x_0,y_0,t)}\right] \\ j_e(x_d,y_d,t) = AT(x_d,y_d,t)^2 \exp\left[\dfrac{-ew_{ei}}{kT(x_d,y_d,t)}\right]\exp\left[\dfrac{e\sqrt{\dfrac{eE(x_d,y_d,t)}{4\pi\varepsilon}}}{kT(x_d,y_d,t)}\right] \end{cases} \tag{7}$$

where $j_h(x_0, y_0, t)$ and $j_e(x_d, y_d, t)$ are the injection current densities for holes and electrons at copper trace which is connected to positive high voltage and ground, respectively, t is the time, E is the local electric field, A is the Richardson constant, T is the temperature, e is the elementary charge, k is the Boltzmann constant, w_{hi} and w_{ei} are the injection barriers for holes and electrons, and ε is the permittivity of the insulation. When holes and electrons reach the opposite electrodes, they are partially blocked at the interface due to the barriers, which can be described as equation (8), where C_h and C_e are the extraction coefficients, all for holes and electrons respectively.

$$\begin{cases} j_h(r_d,z_d,t) = C_h \mu_h n_{h\mu}(r_d,z_d,t)E(r_d,z_d,t) \\ j_e(r_0,z_0,t) = C_e \mu_e n_{e\mu}(r_0,z_0,t)E(r_0,z_0,t) \end{cases} \tag{8}$$

As for trapping process, the trapping rate of various trap depth is depicted as [20, 21]:

$$\frac{dn_t}{dt} = Sv_\mu n_t(n_{ot} - n_t) \tag{9}$$

where S is capture cross-section area, v_μ is drift velocity, n_t is trapped charge density, and n_{ot} is trap density. In equation (6), B_h and B_e have the same effect as Sv_μ. As for detrapping coefficients D_e and D_h [20, 21]:

$$D_{e,h} = v_0 \exp\left(-\frac{E_t}{kT}\right) \tag{10}$$

where v_0 is the attempt to escape frequency, which has been set to $6.2\times10^{12}\text{s}^{-1}$ at room temperature; T is the temperature; k is the Boltzmann constant; E_t is the trap depth. Details of the bipolar charge transport model can be referred to [21].

(2). Parameters derivation and discussion

The simulation is run in the *COMSOL* software with the custom-defined partial differential equations and solved with FEM. The solver is MUltifrontal Massively Parallel Sparse direct Solver (MUMPS), *Electrostatics* and *Coefficient Form PDE* physics models are fully coupled and used. The bipolar charge transport equations are defined in the PDE model and the mobile/trapped electrons/holes are calculated by this model. The charge distribution is also shared with the Electrostatics model and the electric field distribution is calculated by Poisson's equation. The flow chart of the simulation is shown in Fig. 14.

Some parameters that are related to the packaging dielectric properties are derived from experiments. The other parameters that cannot be extracted from experiments are from previous literature and theoretical calculations. Specifically, key parameters determining space charge behavior such as carrier mobility μ and trap depth E_t are obtained from conductivity measurement and isothermal relaxation current measurement on the used silicone encapsulant. Regarding the carrier mobility estimation, according to the space-charge-limited current (SCLC) theory, when the electric field increases and the amount of injected carrier exceeds the trap density, the injected carriers travel in the conduction band. The relationship between the current density and applied voltage follows the Child law, and the conductivity is only related to the carrier mobility [22].

$$\mu = \frac{8 j_c d^3}{9V^2\varepsilon} \tag{11}$$

where μ is carrier mobility, j_c is current density, d is thickness of the tested sample, V is applied voltage, and ε is permittivity. The measured conduction current of the silicone encapsulant is used to derive the mobility as 5×10^{-14} $\text{m}^2\text{V}^{-1}\text{s}^{-1}$. According to Einstein's equation, the diffusion coefficient of carriers, mobility, and temperature agrees to the following relationship:

$$D_f = \frac{\mu kT}{e} \tag{12}$$

where D_f is the diffusion coefficient of carriers, μ is the mobility of carriers, k is Boltzmann's constant, T is the absolute temperature, and e is the amount of elementary charge. Regarding the trap depth estimation, isothermal relaxation current contains lots of information about traps. When the

This article has been accepted for publication in a future issue of this journal, but has not been fully edited. Content may change prior to final publication. Citation information: DOI 10.1109/TPEL.2021.3072655, IEEE Transactions on Power Electronics

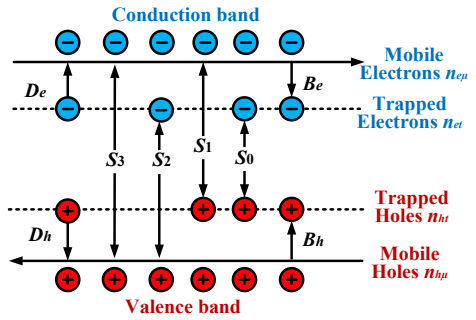

Fig. 13. Schematic of charge trapping, detrapping, and recombination

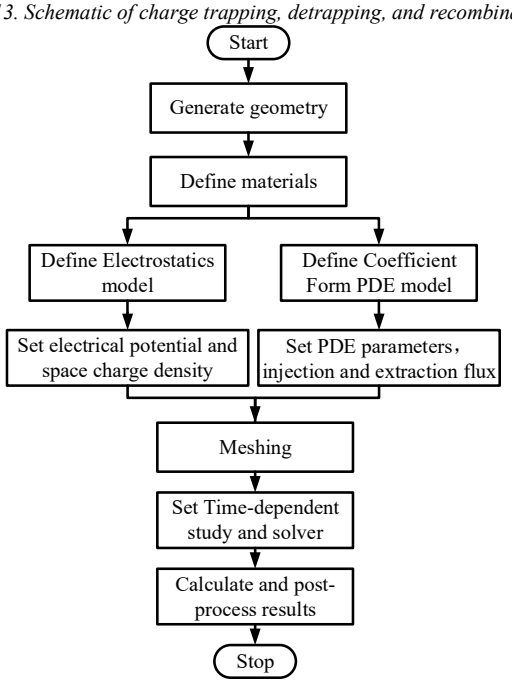

Fig. 14. Flowchart of the bipolar charge transport-FEM space charge simulation

tested silicone sample is electrically stressed, charges are accumulated in the insulation. During the short-circuit stage, the charges detrap and cause relaxation current. The charges detrap according to the law [23]:

$$n = n_0 \exp(-\beta t) = n_0 \exp[-N_c \nu S \exp(-\frac{E_t}{kT})t] \quad (13)$$

where n_0 is the initial trapped charge density, β is the attenuation constant, N_c is the state density of conduction band, v is the thermal motion velocity, S is the cross-section area of the trap, E_t is the trap depth, k is the Boltzmann constant, and T is the temperature. There are two types of traps existing in the tested silicone sample, one is the kind with shallow depth controlling mobility, and the other is the kind with deep depth. Therefore, the isothermal relaxation current can be depicted as [23]:

$$I = \sum_{i=1}^{2} \frac{dn_i}{dt} = -[\beta_1 n_{01} \exp(-\beta_1 t) + \beta_2 n_{02} \exp(-\beta_2 t)] \quad (14)$$

Thus, after fitting the relaxation current, β_1, β_2, n_{01}, and n_{02} can be obtained. According to the expression of β in equation (13), the trap depth of either kind of traps is [23]:

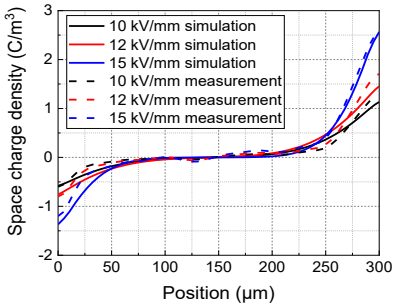

Fig. 15. Comparison between space charge simulation and measurement results of silicone encapsulant

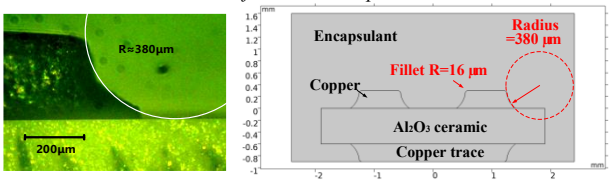

(a) (b)

Fig. 16. Simulation model (a) cross-section of tested substrate (b) FEM model in the simulation

TABLE III
PARAMETERS OF SPACE CHARGE SIMULATION [24, 25]

Parameters	Values	Parameters	Values
W_{hi}	1.15 eV	W_{ei}	1.14 eV
μ_h, μ_e	5×10^{-14} $m^2V^{-1}s^{-1}$	D_{fh}, D_{fe}	1.3×10^{-15} m^2s^{-1}
B_h, B_e	0.05 s^{-1}	n_{oht}, n_{oet}	100 $C\cdot m^{-3}$
S_0, S_1, S_2	4×10^{-3} $m^3\cdot C\cdot s^{-1}$	S_3	0 $m^3\cdot C\cdot s^{-1}$
E_t	1.04 eV	D_h, D_e	3.2×10^{-5} s^{-1}
C_h,C_e	0.9	T	303 K

$$E_t = -kT \ln(\frac{\beta}{N_c \nu S}) \quad (15)$$

The deep trap depth is experimentally evaluated as 1.05 eV according to equation (15). The parameters used in the simulation are shown in Table III [24, 25].

It should be noted that the space charge accumulation is not only related to the electrical properties of the material but also related to the insulation geometry, which affects the baseline electric field distribution and hence affecting the charge behavior. The electric field distribution is then modified by the space charge accumulation, which is not only related to the quantity of accumulated charge but also related to its polarity and spatial distribution.

Generally, mobility is one of the main reasons to determine the transport speed of the charges since the drift velocity of the charges can be expressed as:

$$v_\mu = \mu E \quad (16)$$

where E is the local electric field and μ is the mobility. If other parameters are kept the same, the higher the drift velocity, the more broadly the space charge is distributed. However, the local electric field also plays a significant role in charge transport as manifested in equation (16).

In terms of the effect of trap depth on space charge behavior, it can be analyzed by two aspects. Studies have shown that chemical impurities in the crystal lattice lead to discrete trapping energy levels, and the incompleteness of the crystal

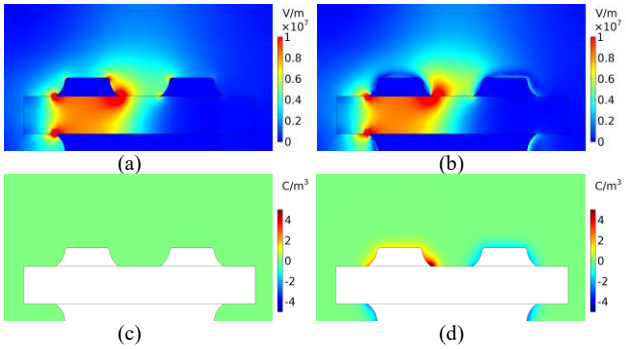

Fig. 17. Space charge simulation results under DC voltage. (a) electric field distribution at 1 s (b) electric field distribution at 1800 s (c) space charge distribution at 1 s (d) space charge distribution at 1800 s

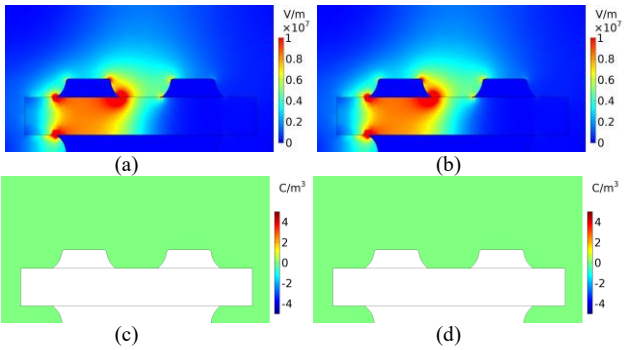

Fig. 18. Space charge simulation results under square pulses. (a) electric field distribution at 1 s (b) electric field distribution at 1800 s (c) space charge distribution at 1 s (d) space charge distribution at 1800 s

structure is the cause of the quasi-continuous distribution of traps [26]. The traps inside materials can be roughly divided into two types, one is traps formed by physical defects (generally shallow and influence mobility), and the other is traps formed by chemical defects (generally deep and constrain charges). According to equation (13) that describes detrapping principle, the deeper the trap depth, the harder the charges escape, which in turn increases accumulated space charges.

(3). Model verification and application

To verify these parameters, space charge simulation on the silicone encapsulant film sample with the same properties is performed and compared with experiment results, as shown in Fig. 15. It is observed that the space charge distribution of simulation results is quite similar to that of experimental results under different applied fields. Therefore, these parameters can be used to simulate the space charge dynamics with the bipolar charge transport model.

A FEM model with the same structure as that of actual power module packaging is built in the software, as presented in Fig. 16. The copper traces with 0.3 mm thickness are attached on both sides of the substrate. The Al_2O_3 ceramic layer with 0.6 thickness separates the copper traces. The substrate is enclosed with the silicone encapsulant. One of the copper traces on the top side of the substrate is applied either 5000 V DC or square pulse. The other one on the top side and the copper trace at the bottom are grounded. The distance between the copper traces on the top side is simulated from 0.35 to 0.8 mm. Simulation results of 0.35 mm distance are shown as an example in Fig. 17 and 19. In the DC situation, with the accumulation of space

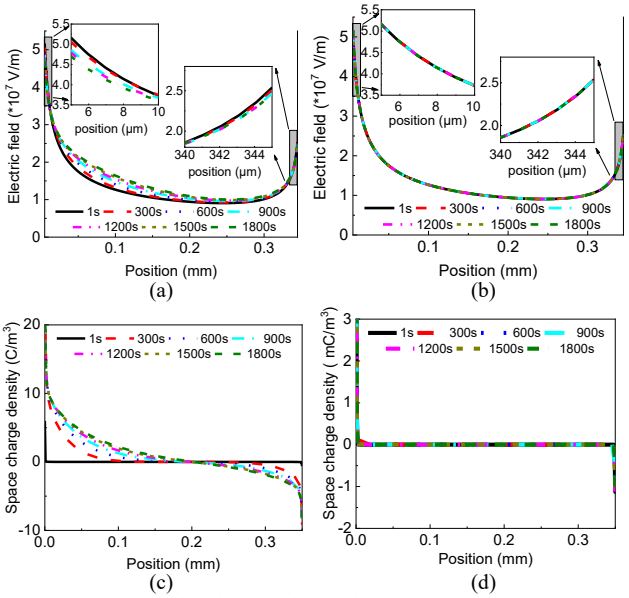

Fig. 19. Electric field and space charge distribution along the bottom line between copper traces. (a) electric field distribution under DC (b) electric field distribution under square pulses (c) space charge distribution under DC (d) space charge distribution under square pulses

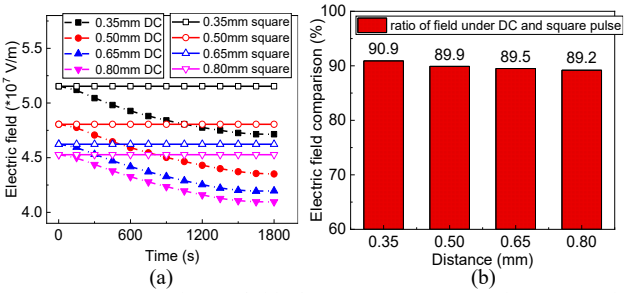

Fig. 20. Maximum electric field of various copper trace distances under 5000 V DC and square pulses. (a) maximum electric field with time (b) maximum field comparison between DC and square pulse situations

charge, the electric field decreases at the triple-point area but increases between the upper traces. However, space charge accumulation is hardly seen in the square pulse situation even after long time applications.

To compare the maximum electric field in different situations, the electric field and space charge distribution along the line between the bottom edges of copper traces at the top side are plotted in Fig. 19. The maximum electric field at the triple-point gradually decreases with the space charge accumulation under DC voltage, whereas the field keeps stable under square pulses since no obvious space charges are accumulated. The charges under square pulse are shortly injected and immediately extracted or decayed when the square voltage is off, hence the space charge accumulation is limited compared to that under DC. The maximum electric field under DC is ~90% of that under square pulses when the space charge distribution is stable, as shown in Fig. 20. The maximum electric field results considering space charge accumulation agree with the PDIV measurement results under DC and square pulses in section II. It should be noted that the homocharge effect in this study is not the only effect that space charge accumulation may have. As demonstrated in Fig. 12, the electric field between the positive

This article has been accepted for publication in a future issue of this journal, but has not been fully edited. Content may change prior to final publication. Citation information: DOI 10.1109/TPEL.2021.3072655, IEEE Transactions on Power Electronics

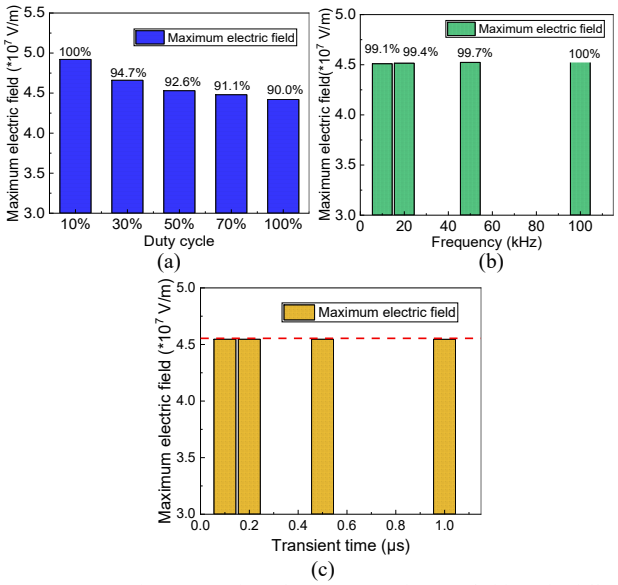

Fig. 21. Simulation results of maximum electric field with different parameters of square wave. (a) effect of duty cycle (b) effect of switching frequency (c) effect of transient time

and negative charges increases with the approaching of the injected charges. Therefore, space charge accumulation may lead to electric field increase and threaten reliability depending on the charge distribution.

C. Effect of Square Wave Parameters on Electric Field Distortion

To provide more information about the factors that may influence space charge accumulation and electric field distribution, the effect of square wave parameters (duty cycle, switching frequency, and transient time) on the maximum electric field in the packaging insulation is simulated considering space charge accumulation. The simulation results are shown in Fig. 21. It is found the maximum field decreases with the increase of duty cycle, which is quite straightforward since the larger the duty cycle, the more similar the square wave to DC. With the increase of duty cycle, the ratio of the charge injection and transport time to charge decay time increases. Therefore, more charges will be accumulated and the effect of space charge around the metal corner becomes more prominent. Regarding the switching frequency effect, it is not as apparent as that of duty cycle. The change of maximum electric field in the packaging insulation is not obvious with different switching frequencies under the same duty cycle. It is because the variation of switching frequency just influences the alternating time of voltage-on and voltage-off state, the ratio of the charge injection and transport time to charge decay time does not change. As for the transient time, the simulation results manifest that the maximum electric field in the packaging insulation seems do not change much with different transient time from 100 ns to 1 μs. It is quite understandable that compared with the duration of voltage application, the transient time is less significant for charge injection and transportation, thus has less effect on electric field distortion. However, it should be noted that the transient time of square wave still can influence the characteristics of partial discharge by changing the process of partial discharge (carrier collision, electron emission, and avalanche, etc) but not in the way of space charge accumulation. Further investigation about the partial discharge characteristics and the influencing factors including electrical stress parameters and insulation geometry will be reported in future papers.

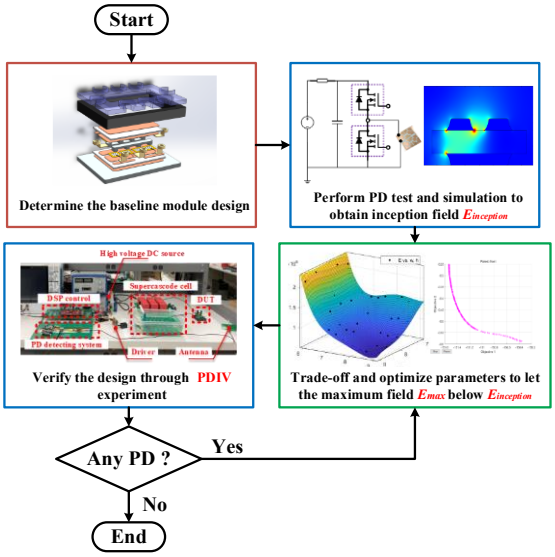

Fig. 22. Design procedure for high-voltage module packaging insulation

D. Power Module Packaging Insulation Design Procedure

To sum up, the space charge accumulation makes the maximum electric field under DC smaller than that under square pulses, which thereby affects the PDIV values. The current high-voltage power module packaging design has several drawbacks. It does not consider the effect of space charge, the maximum electric field is derived from either electrostatic or conduction simulation. Besides, the generally used design criterion is to compare the maximum electric field from the simulation with the breakdown strength offered by insulation material manufacturers. The breakdown strength provided by the manufacturer is obtained from the experiment under uniformly distributed electric field such as plate-to-plate electrode setup defined by standards. This strength may not agree with experimental results. Therefore, the PD experiment and electric field simulation considering space charge should be combined to derive a criterion for high-voltage power module packaging insulation design, which is shown in Fig. 22.

Step 1. Determine baseline design

Before deciding detailed insulation parameters, a baseline design should be determined according to the requirement of the thermal and electrical performance of the module. Specifications such as the general packaging structure and insulating material should be chosen. These specifications are usually predefined or can refer to existing commercial products.

Step 2. Perform PD experiment and electric field simulation considering space charge accumulation

After determining the baseline design, the PD experiment with the same electric stress as that at actual operation condition

should be performed to obtain PDIV. The PDIV is applied to the FEM model considering space charge accumulation and to obtain the maximum electric field. These data are fitted to derive a PD inception field as a criterion to determine the packaging parameters (in this study, the inception field is ~45 kV/mm which is different from 30 kV/mm provided by the manufacturer which is derived from the breakdown experiment in an evenly distributed electric field).

Step 3. Optimization of the insulation parameters

The detailed parameters such as the thickness of the insulation, the gap distance between two neighboring copper traces, and the clearance of outside terminals should be determined by the criterion that the maximum field should be smaller than the PD inception field. Besides, the parameters sometimes need to be optimized considering manufacturing errors or trade-off between electrical and thermal performances.

Step 4. Experimental verification

After optimization, the new packaging samples with the optimized parameters should be verified without PD with the rated electric stress through PD experiments. If the PDIV is still lower than the rated voltage, an extra margin should be given for another round of optimization until it passes the verification. The application of this procedure will be reported in the future due to the limited space here.

VI. Conclusion

PD of high-voltage power module under DC and PWM waves are investigated by a proposed high dV/dt PD testing platform that involves SHF-down-mixing PD detection and a high-voltage scalable square wave generator. Space charge measurement and modeling are used to explain PDIV difference under DC and PWM excitations and to update the high-voltage power module insulation design procedure.

(1). The proposed PD detection platform can avoid electromagnetic interference and is capable of detecting PD signals at the rising and falling edges of PWM waves. The SHF-down-mixing method is contactless and highly immune to electromagnetic interference which makes it suitable for PD detection of power module packaging.

(2). The PDIV of power module insulation under PWM waves is less than that under DC voltage for the same packaging structure. Space charge testing and modeling results show that charges are prone to be accumulated in silicone encapsulant and lead to local electric field distortion, which agrees with the PDIV results. It should be noted that the space charge accumulation also can lead to electric field concentration and poses threat to reliability, which will be thoroughly explored and reported in the future. Based on this model, a tentative packaging insulation design procedure combining experimental and simulation results is proposed to facilitate the high-voltage power module insulation design process.

Acknowledgment

The authors would like to express their appreciation to National Science Foundation for lending its financial support under award #1846917.

References

[1] L. Zhang, X. Yuan, X. Wu, *et al*, "Performance Evaluation of High-Power SiC MOSFET Modules in Comparison to Si IGBT Modules," *IEEE Trans. Power Electron.*, vol. 34, no. 2, pp. 1181-1196, Feb. 2019.

[2] D. Fabiani, G. C. Montanari, A. Cavallini, *et al*, "Relation between space charge accumulation and partial discharge activity in enameled wires under PWM-like voltage waveforms," *IEEE Trans. Dielectr. Electr. Insul.*, vol. 11, no. 3, pp. 393-405, June 2004.

[3] C. Gao, Y. Xu, J. Wang, *et al*, "Partial Discharge Online Monitoring and Localization for Critical Air Gaps Among SiC-Based Medium-Voltage Converter Prototype," *IEEE Trans. Power Electron.*, vol. 34, no. 12, pp. 11725-11735, Dec. 2019.

[4] C. Zhang, Y. Xu, M. Dong, *et al*, "Design and Assessment of External Insulation for Critical Components in a Medium Voltage SiC-Based Converter via Optical Method," *IEEE Trans. Power Electron.*, (Early access).

[5] H. You, Z. Wei, M. Aldawsari, *et al*, "Partial Discharge Behaviors in Power Module under Very High Dv/dt Repetitive Square Voltages," in *IEEE Electr. Insul. Conf. (EIC)*, Calgary, AB, Canada, 2019, pp. 489-492.

[6] J. K. Nelson, *Dielectric polymer nanocomposites*, New York, NY, USA, Springer, 2010.

[7] Y. Wang, J. Wu, S. Yi, *et al*, "Research of simultaneous measurement of space charge and conduction current in cross-linked polyethylene," in *Int. Conf. Cond. Monit. and Diagn. (ICCMD)*, 2016, pp. 78-81.

[8] Y. Wang, J. Wu, and Y. Yin, "Space charge behavior in low density polyethylene at low temperatures," *IEEE Trans. Dielectr. Electr. Insul.*, vol. 24, no. 6, pp. 3860-3868, 2017.

[9] Y. Wang, J. Wu and Y. Yin, "Investigation of surface trap distribution in LDPE/SiO2 nanocomposite based on simultaneous observation of space charge and relaxation current," *IEEE Trans. Dielectr. Electr. Insul.*, vol. 23, no. 6, pp. 3486-3493, Dec. 2016.

[10] M. Tousi and M. Ghassemi, "Characterization of Nonlinear Field-Dependent Conductivity Layer Coupled With Protruding Substrate to Address High Electric Field Issue Within High-Voltage High-Density Wide Bandgap Power Modules," *IEEE Trans. Emerg. Sel. Topics Power Electron.*, vol. 8, no. 1, pp. 343-350, March 2020.

[11] G. Mitic and G. Lefranc, "Localization of electrical-insulation and partial-discharge failures of IGBT modules," *IEEE Trans. Ind. Appl.*, vol. 38, no. 1, pp. 175-180, Jan.-Feb. 2002.

[12] X. Song, A. Huang, S. Sen, *et al*, "15-kV/40-A FREEDM Supercascode: A Cost-Effective SiC High-Voltage and High-Frequency Power Switch," *IEEE Trans. Ind. Appl.*, vol. 53, no. 6, pp. 5715-5727, Nov. 2017.

[13] J. Biela, D. Aggeler, D. Bortis, *et al*, "Balancing Circuit for a 5-kV/50-ns Pulsed-Power Switch Based on SiC-JFET Super Cascode," *IEEE Trans. Plasm. Sci.*, vol. 40, no. 10, pp. 2554-2560, Oct. 2012.

[14] X. Li, H. Zhang, P. Alexandrov, *et al*, "Medium voltage power switch based on SiC JFETs," in *IEEE Appl. Pow. Electron. Conf. Exp. (APEC)*, Long Beach, CA, 2016, pp. 2973-2980.

[15] C. Poynton, *Digital video and HD: Algorithms and Interfaces*. Elsevier, Waltham, MA, USA, 2012.

[16] R, Patel, S. Yeboah, R. light, and M. Clark, "Ultrastable heterodyne interferometer system using a CMOS modulated light camera," *Optics Express*, vol. 20, no. 16, pp. 17722-17733, 2012.

[17] H. You, Z. Wei, B. Hu, *et al*, "Partial Discharge Behaviors in Power Modules under Square Pulses with Ultra-fast Dv/dt," *IEEE Trans. Power Electron.*, (Early access).

[18] S. Coenen, S. Tenbohlen, S. M. Markalous and T. Strehl, "Sensitivity of UHF PD measurements in power transformers," *IEEE Trans. Dielectr. Electr. Insul.*, vol. 15, no. 6, pp. 1553-1558, December 2008.

[19] Y. Wang, X.Yi, Y. Wang, et al., "Partial-Discharge-Free Insulation Design of Air-Core Permanent Magnet Synchronous Machine for Aircraft Propulsion," *IEEE Trans. Transport. Electrific.*, (Early access).

[20] Y. Wang, J. Wu and Y. Yin, "Relationship between space charge behavior and trap energy density distribution: A simultaneous measurement," *IEEE Trans. Dielectr. Electr. Insul.*, vol. 26, no. 3, pp. 738-745, 2019.

[21] J. M. Alison and R. M. Hill, "A model for bipolar charge transport, trapping and recombination in degassed crosslinked polyethene," *J. Phys. D. Appl. Phys.*, vol. 27, no. 6, pp. 1291-1299, Jun. 1994.

[22] A. Rose, "Space-charge-limited currents in solids," *Phys. Rev.*, vol. 97, no. 6, pp. 1538, 1955.

[23] G. Chen, Z. Xu. "Charge trapping and detrapping in polymeric materials, " *J. Appl. Phys*, vol.106, pp.123707, 2009.

[24] Y. Wang, J. Wu and Y. Yin, "A space-charge and relaxation-current based method for estimating electron and hole trap energy distribution," *IEEE Trans. Dielectr. Electr. Insul.*, vol. 24, no. 6, pp. 3839-3848, Dec. 2017.

[25] Y. Wang, J. Wu, Y. Yin, et al, "Effect of micro and nano-size boron nitride and silicon carbide on thermal properties and partial discharge resistance of silicone elastomer composite," *IEEE Trans. Dielectr. Electr. Insul.*, vol. 27, no. 2, pp. 377-385, April 2020.

[26] M. Roy, J. Nelson, R. MacCrone, et al. "Candidate mechanisms controlling the electrical characteristics of silica/XLPE nanodielectrics," *J. Mat. Sci.*, vol. 42, no. 11, pp. 3789-3799, 2007.